

THE EFFECTS OF LOCALIZED DAMPING ON STRUCTURAL RESPONSE

D. H. Merchant, R. M. Gates,
Boeing Aerospace Company

M. W. Ice, and J. W. VanDerlinden
Boeing Computer Services, Inc.

SUMMARY

The effect of localized structural damping on the excitability of higher order normal modes of the Large Space Telescope is investigated. A preprocessor computer program was developed to incorporate Voigt structural joint damping models in a NASTRAN finite-element dynamic model. A postprocessor computer program was developed to select critical modes for (1) low-frequency attitude-control problems and for (2) higher frequency fine-stabilization problems. The mode selection is accomplished by ranking the flexible modes based on (1) coefficients for rate gyro, position gyro, and optical sensors and on (2) image-plane motions due to sinusoidal or random power spectral density force and torque inputs.

INTRODUCTION

The presence of distributed damping in spacecraft structures may significantly affect the predicted dynamic response of higher order normal modes. The purpose of this study was to develop and implement a general methodology framework for evaluating the effects of distributed structural damping on spacecraft structures. Identification of potential limitations in the conventional use of uncoupled normal modes for structural dynamic response analyses has resulted from the application of this methodology to the Large Space Telescope (LST) control system design (reference 1).

The methodology is concerned with two general aspects: (1) including distributed damping in a finite-element structural model and (2) selecting critical modes for subsequent dynamic analyses and assessing the effects of modal velocity coupling. Methodology for modeling distributed damping in a NASTRAN structural model was developed and implemented in a preprocessor computer program used to generate the required NASTRAN BULK DATA. This computer program was developed for convenience in preparing NASTRAN input, and its use is strictly optional. Methodology for selecting critical modes and assessing modal coupling was developed and implemented in a post-processor computer program. Application of this methodology to the LST control and fine-stabilization problems was accomplished using a detailed LST NASTRAN structural model. Qualitative results and conclusions of the present study are discussed.

STRUCTURAL JOINT MODELING

Structural damping is comprised of both material (hysteretic) damping and energy dissipation in structural joints. Material damping may be represented in linear dynamic response analyses by uncoupled modal viscous damping ratios (ζ). Energy dissipation in structural joints is a nonlinear function of many parameters (references 2, 3, 4, 5, and 6). However, this phenomenon must also be represented by linear models so that linear analysis techniques may be used. Two linear joint models have been used to describe the frequency-dependent effects of distributed joint damping: the Maxwell model and the Voigt model. The three-parameter anelastic model, referred to as the Maxwell model, has been identified in the literature (references 2, 4, 5, 6, and 7) as a feasible model for representing hysteretic damping in materials. For a massless structural element and joint supporting a single mass, the Maxwell and Voigt models are essentially equivalent. Since the two-parameter Voigt model is simpler than the three-parameter Maxwell model, the Voigt model is used in the application to the LST control and vibration studies.

The two-parameter Voigt unit, shown schematically in Figure 1, consists of a spring in parallel with a viscous damper. It is the simplest complex-notation model and possesses hysteretic properties characteristic of damping in materials and structural joints. For sinusoidal excitation, the equivalent damping and stiffness coefficients (C_T and K_T) for the Voigt model, in series with a spring, are functions both of the structural parameters (K, K_V, C) and of the forcing frequency (β):

$$C_T = \frac{C K^2}{(K+K_V)^2 + C^2 \beta^2} \quad (1)$$

$$K_T = \frac{K K_V (K+K_V) + C^2 \beta^2 K}{(K+K_V)^2 + C^2 \beta^2} \quad (2)$$

These coefficients are determined for the single degree-of-freedom system shown in Figure 1 using Laplace transforms.

For very low frequencies,

$$C_T(\beta=0) = C \left(\frac{K}{K+K_V} \right)^2 \quad (3)$$

$$K_T(\beta=0) = K_V \left(\frac{K}{K+K_V} \right) \quad (4)$$

Equation (4) indicates that, at very low frequencies, the total Voigt joint/member stiffness coefficient is the static stiffness of the series spring arrangement.

For very high frequencies,

$$C_T(\beta=\infty) = 0 \quad (5)$$

$$K_T(\beta=\infty) = K \quad (6)$$

Equations (5) and (6) indicate that at very high frequencies the damper effectively becomes rigid; thus, the total Voigt joint/member damping coefficient is zero and the total stiffness coefficient is the member stiffness.

A preprocessor computer program was written to implement this methodology by adding structural joint models to a NASTRAN finite-element structural model. The preprocessor modifies the input data for a conventional finite-element structural model and generates additional inputs necessary to incorporate the Voigt joint damping model at the ends of specified BAR or ROD elements. The damping characteristics of the joints are modeled with the NASTRAN linear viscous damping element (VISC). The preprocessor is presently limited to incorporating joint damping at the ends of BAR and ROD elements defined in a rectangular coordinate system.

Schematics of NASTRAN BAR and ROD elements with joint damping models included at one end are shown in Figure 2. The original element lies between gridpoints a and b. When the user requests a joint damping model to be included at gridpoint a, the preprocessor establishes the model as follows:

- a. Gridpoint c is introduced on the BAR (ROD) axis at a specified distance from gridpoint a.
- b. Properties of the BAR (ROD) between gridpoints a and c are altered as specified, either by direct input or by default values, to provide desired stiffness characteristics.
- c. For a BAR element, gridpoints e and f are established such that gridpoints a, b, e and f form an orthogonal axis system at gridpoint a. Gridpoint e is in plane 1 of the BAR element, and gridpoint f is in plane 2. The distances from gridpoint a to gridpoints c, e and f are identical.
- d. Viscous damping (VISC) elements (m, n and p) with desired properties are inserted between gridpoints a and c, a and e, and a and f for a BAR element and between a and c only for a ROD element. The VISC elements used with BAR and ROD elements may have translational damping components, in addition to the rotational components, only when the VISC element axis is aligned with an axis of the displacement coordinate system.
- e. For a BAR element, gridpoints e and f are multipoint-constrained to gridpoint c.

The VISC element provides damping along its axis and in torsion about its axis. Therefore, for a BAR element, three VISC elements are required at each gridpoint to provide damping of all six degrees of freedom. The locations of gridpoints e and f in Figure 2(a) are calculated, in the rectangular coordinate system, by vector analysis.

Default values are automatically specified by the preprocessor for the NASTRAN data describing the structural joints. The default value specifying joint length results in a joint member whose length is ten percent of the original element length. The default values specifying joint member area, moments of inertia, and torsional constant are calculated to give a ten percent reduction in axial, bending, and torsional stiffnesses for a cantilever beam. This stiffness reduction results in a five percent reduction in the first resonant frequency for a massless cantilever beam with a concentrated mass at the tip. The five percent frequency reduction is consistent with the lower values measured from actual hardware compared with values predicted from standard finite-element analysis techniques.

The VISC elements and parameters chosen to define the joint damping characteristics must result in a physical damping matrix which satisfies kinematic compatibility. The compatibility relations for the damping matrix are represented by

$$[BGG]\{\phi_R\} = \{0\}$$

where $[BGG]$ is the NASTRAN viscous damping matrix in physical coordinates, and $\{\phi_R\}$ is an arbitrary vector of rigid-body translations and rotations. Equation (7) ensures that no damping forces are generated by rigid-body motions. With regard to kinematic compatibility, the NASTRAN VISC damping element is limited to two applications:

- a. With translational damping, the compatibility relations are satisfied only when the axis of the VISC element is aligned with an axis of the displacement coordinate system.
- b. Without translational damping, the compatibility relations involving only rotational damping are satisfied for any orientation of the VISC element.

For the general case of an arbitrarily oriented element having both translational and rotational damping components, the present NASTRAN VISC element does not provide the translation/rotation damping coupling terms required by Equation (7).

MODE SELECTION

Critical mode selection is accomplished by the postprocessor computer program using structural dynamic characteristics, including the coupled modal damping matrix, obtained from the NASTRAN restart tape. The NASTRAN calculation of the modal damping matrix is accomplished with DAMP ALTER statements in the NASTRAN EXECUTIVE CONTROL deck. The postprocessor has two major options. It will select critical modes for (1) low-frequency control problems involving sinusoidal analysis and (2) higher frequency fine-stabilization problems involving either sinusoidal or random vibration analysis. The methodology determines the critical normal modes in the low-frequency control range by comparing control-system coefficients associated with optical sensors as well as with rate and position gyro sensors. In the higher frequency fine-stabilization range, the methodology determines the critical normal modes by estimating the image-plane motion due to specified sinusoidal or random power spectral density (PSD) force and torque inputs. These calculations for ranking the modes use only the diagonal terms of the coupled modal damping matrix. The significance of the neglected damping coupling terms is therefore evaluated numerically in a separate series of calculations. The capability to convert between different systems of units is also available; the postprocessor input may be provided in the inch- $\frac{\text{pound}\cdot\text{second}^2}{\text{inch}}$ -second system or FSS (foot-slug-second) system and the output can be converted to the FSS or MKS (meter-kilogram-second) system. The general logic flow of the postprocessor is shown in Figure 3.

Low-Frequency Control Option

For the control option, the postprocessor reads the following structural dynamic characteristics from the NASTRAN checkpoint/restart tape:

- [ϕ] the matrix of mode shapes for selected modes and freedoms
- {M} the matrix of generalized masses for selected modes
- [D] the matrix of generalized coupled modal damping terms for selected modes
- { ω } the matrix of modal frequencies for selected modes

The optical amplification matrix, [B_0], and grid I.D.'s of image train components are input to the postprocessor by punched cards. The optical amplification matrix describes the three translations of the image plane in terms of physical translations and rotations of the image train components.

The coupled modal damping matrix is calculated by applying the modal transformation to the viscous damping matrix [BGG] generated by NASTRAN in physical coordinates

$$[D] = [\phi]^T [BGG] [\phi] = [BHH] \quad (8)$$

The DMAP ALTER statements used to calculate and output the coupled damping matrix are included in the EXECUTIVE CONTROL deck as shown in Table 1.

Equivalent modal viscous damping (ζ_i) is calculated from the coupled modal damping matrix as follows:

$$\zeta_i = \frac{D_{ii}}{2 \omega_i M_i} \quad (9)$$

Rate or position coefficients for each requested mode are calculated for the selected freedoms and image plane motions as follows:

$$R(3014, 3024)_j = \frac{\phi_{3014,j} \phi_{3024,j}}{(2\zeta_j) \omega_j M_j} \quad (1)$$

$$P(3014, 3022)_j = \frac{\phi_{3014,j} \phi_{3022,j}}{(2\zeta_j) \omega_j^2 M_j} \quad (1)$$

$$P(3014, \quad)_j = [B_o] \{ \phi_j^B \} \frac{\phi_{3014,j}}{(2\zeta_j) \omega_j^2 M_j} \quad (1)$$

where R and P denote rate and position coefficients, respectively. Grid-point freedoms for the input point and response point are specified in parentheses. The last digit of each I.D. is the input or output freedom specified at the gridpoint indicated by the preceding digits. For example, P(3014, 3022)_j requests a position coefficient to be calculated for the j^{th} mode at gridpoint 302 in the freedom 2(y) direction due to a unit sinusoidal torque at gridpoint 301 in the freedom 4 (θ_x) direction. The three-component vector of displacement response at the image plane due to a unit sinusoidal torque at gridpoint 301 in the freedom 4 (θ_x) direction is calculated as shown in Equation (12). Position and rate coefficients for all selected modes are ranked and listed along with their mode numbers and frequencies.

High-Frequency Fine-Stabilization Option

For the fine-stabilization option, as with the low-frequency control option, the structural dynamic characteristics $[\phi]$, $[M]$, $[D]$ and $\{\omega\}$ for selected modes and freedoms are read from the NASTRAN checkpoint/restart file, and the optical amplification matrix $[B_o]$ and grid I.D.'s of the image train components are input by cards. Equivalent modal viscous damping coefficients are calculated using Equation (9).

The inputs unique to this option are tables of sinusoidal peak or PSD force and torque levels versus frequency which are used in the sinusoidal and random analyses, respectively. Since the phase relationships among the sinusoidal force and torque inputs are not well defined, the generalized force for the j^{th} mode F_j is represented by

$$F_j = \max(|\phi_{ji}^F| * F_i) \quad (13)$$

where ϕ_{ji}^F is the j^{th} mode shape at the i^{th} forced freedom, and

F_i is the peak force (or torque) of the i^{th} forced freedom at the j^{th} mode frequency

The modal displacement at resonance q for the j^{th} mode is

$$q_j = \frac{F_j}{2\zeta_j \cdot \omega_j^2 \cdot M_j} \quad (14)$$

Physical displacements corresponding to the optical train components for the j^{th} mode are

$$\{x_B\}_j = \{\phi_j^B\} q_j \quad (15)$$

where $\{\phi_j^B\}$ is the j^{th} mode shape vector at the response freedoms corresponding to the optic train components.

Physical displacements of the image at the focal plane for the j^{th} mode are

$$\{x_1\}_j = [B_o] \{x_B\}_j \quad (16)$$

As previously noted, the optical amplification matrix, $[B_o]$, describes the three translations of the image plane in terms of physical translations and rotations of the image train components.

For random force (or torque) inputs, the RMS modal displacements for the j^{th} mode are

$$(q_j)_{\text{RMS}} = \frac{1}{2\zeta_j \cdot \omega_j^2 \cdot M_j} (\pi f_j S_j \zeta_j)^{\frac{1}{2}} \quad (17)$$

where $S_j = \{\phi_j^F\}^T [S_F(f_j)] \{\phi_j^F\} = \sum_i (\phi_{ij}^F)^2 \cdot S_{Fi}(f_j)$

and $S_{Fi}(f_j)$ is the input force (torque) power spectrum at the i^{th} input freedom for frequency f_j

The individual input force PSD's, defined with frequency (f) in Hz, are assumed approximately constant within $\pm 20\zeta_j f_j$ of the j^{th} modal frequency. This frequency band accounts for approximately 98 percent of the RMS modal displacement for a constant PSD. No cross-spectra are assumed so that $[S_F(f_j)]$ is a diagonal matrix constructed, for each frequency, from one value of force PSD and one value of torque PSD.

Equations (15) and (16) are then used to calculate RMS values of physical displacements (x_B) and displacements of the image at the focal plane (x_1) for each mode. These calculated RMS displacements are ranked and listed along with their mode numbers and frequencies.

The degree of modal velocity coupling is calculated as the ratio of coupled to uncoupled response for all modes having potentially significant coupling. These modes are identified by numerically considering both the relative magnitudes of each pair of off-diagonal and diagonal damping terms and the proximity of the modal frequencies corresponding to these pairs of damping terms. To assess the degree of modal velocity coupling, the ratio of coupled response to uncoupled response is calculated and output for all modes selected as having potentially significant coupling. The coupled response is calculated for each mode using the admittance matrix at the resonant frequency and unit forces applied at selected gridpoints.

LST STRUCTURAL MODEL

The basic LST structural dynamics model (Model 1) includes detailed modeling of the Support Systems Module (SSM), the Orbital Telescope Assembly/Science Instruments (OTA/SI) and four deployed appendages. Table 2 shows the detailed breakdown into numbers of gridpoints, structural elements, and dynamic degrees of freedom for the various substructures comprising the complete structural dynamic model. The grid geometry and some of the element connections and gridpoint identifications for the SSM and OTA/SI structural dynamic models are shown in Figures 4 and 5, respectively.

The SSM model, shown in Figure 4, consists of the aft shell, the equipment section including reaction wheels and interface points, the forward shell, and appendages. The aft shell is modeled with coarse-grid plate elements as suggested by Figure 4. Four ring stiffeners, three on the cylinder and one around the access porthole on the aft end, are modeled with BAR elements. The forward end of the aft shell is connected to the smaller diameter inner shell of the equipment section through multipoint constraint equations.

The equipment section inner shell is modeled with 60 plate elements as shown in Figure 4. The equipment bays are formed by three large external ring frames and 15 longerons. These rings and longerons, not shown in the figure, are modeled with 105 BAR elements offset radially approximately one-half the bay depth. The forward gridpoints of the SSM equipment section are connected to the central gridpoint through multipoint constraint equations. Four reaction wheels are each supported by four BAR elements attached to the corners of the forward and aft compartments of the bays as shown in Figure 4. The gridpoints representing the reaction wheels have six dynamic degrees of freedom each. The three SSM interface gridpoints are each supported by two stiff BAR elements which distribute the interface loads to the aft and center ring frames at the intersection with the nearest longeron. These BAR elements are not shown in Figure 4. The forward shell is modeled as a beam consisting of 11 BAR elements cantilevered from the central gridpoint of the forward end of the equipment section.

The deployed high gain antennas (HGA) and solar arrays are modeled as beams consisting of 5 and 9 BAR elements each, respectively. The bases of the appendages are connected to the forward end of the SSM equipment section with 3 rotational and 3 translational scalar spring elements each.

The OTA/SI model, shown in Figure 5, consists of the metering truss including the secondary mirror, the primary support structure including the primary mirror and interface flexures, and the focal plane structure including the science instruments. The graphite/epoxy metering truss is modeled with BAR elements as shown in Figure 5. The secondary mirror is supported by four radial graphite/epoxy beams, each modeled with three BAR elements. The secondary mirror gridpoint, having six degrees of freedom, is connected to the four support points by multipoint constraint equations.

The primary support structure consists of six radial beams connecting inner and outer rings as shown in Figure 5. These beams and rings are modeled with 42 BAR elements. The metering truss is connected to the stiff outer ring with BAR's at 8 points which represent the eight fittings. The three primary mirror support gridpoints are connected to three of the radial beams by three axial bar elements. These three gridpoints are connected to the central primary mirror gridpoint through multipoint constraint equations. The three interface flexures are each modeled by two scalar spring elements, one providing axial stiffness and the other providing tangential stiffness. These scalar elements connect the SSM interface gridpoints to three stiff BAR elements extending radially outward from the OTA/SI primary support ring as shown in Figure 5.

The focal plane structure consists of two hexagonal rings connected by six axial and six diagonal truss members. This assembly is supported from three points on the primary support ring by nine truss members. The three fine guidance sensors are each supported from the focal plane structure by four BAR elements. The star tracker and two gyro sensors are supported by single stiff BAR elements from the primary support ring. The six gridpoints on the aft hexagonal ring of the focal plane structure are connected to a central gridpoint by multipoint constraint equations. This central gridpoint has six dynamic degrees of freedom. A single gridpoint located aft of the focal plane is used to represent the science instruments. A rigid link (multipoint constraint) connects the aft ring gridpoint to the SI gridpoint.

LST Model 1 was modified to include structural joint damping at 26 locations throughout the structure. This modified finite-element model was designated LST Model 2. Some joints were incorporated using the preprocessor and others were added manually. The manual data input was for joints in the basic structural model which were modeled using elements other than BARS or RODS. Voigt models were added at the appendage deployment hinges, the star tracker support, the metering truss supports, the OTA/SSM interface flexures, the SI focal plane structure supports, and the SSM forward shell support. The effects of material damping were included by adding modal viscous damping for all flexible modes to the modal damping matrix corresponding to the Voigt joint models.

The deployment hinges for the four appendages (two high-gain antennas and two solar arrays) in the basic LST model were idealized using scalar spring (ELAS) elements. The Voigt models were generated for the modified LST model by adding DAMP1 elements in parallel with these ELAS elements to provide joint damping in three rotational degrees of freedom. Joint damping characteristics for the star tracker, which is cantilevered from the primary support ring, were also input manually. Scalar damping elements (DAMP1) were used to provide damping in the three rotational directions. Damping in the eight metering truss/primary mirror support ring fittings was modeled using scalar damping (DAMP1) elements in the axial direction only. Damping in the OTA/SSM interface flexures was modeled using axial scalar damping elements in parallel with the axial scalar spring components.

The preprocessor was used to incorporate Voigt structural joint models in the nine BAR elements supporting the SI focal plane structure. The nine VISC elements, with only rotational damping components, were defined at the three gridpoints where the SI connects to the primary support ring. The preprocessor was also used to incorporate a structural joint at the base of the SSM forward shell.

Free-free mode shapes, frequencies, generalized masses, and the coupled modal damping matrix for 100 flexible modes were determined using NASTRAN rigid format 3. Modal frequencies ranged from less than 1 Hz for appendage modes to more than 130 Hz. The coupled modal damping matrix for the Voigt joint damping of LST Model 2 indicated off-diagonal terms frequently exceeding the corresponding diagonal terms, sometimes by as much as an order of magnitude.

RESULTS

The preprocessor and postprocessor methodology was applied to two different LST control system studies: 1) a time-domain control simulation and 2) a frequency-domain vibration analysis. LST fine-stabilization errors induced by the attitude control system cover a wide frequency spectrum from DC up to 300 Hz. In order to analyze the problem efficiently, it was divided into two efforts on the basis of frequency. Although there is some overlap in frequency, the low-frequency control analysis covers DC up to about 20 Hz, and the vibration frequency analysis covers from 10 Hz to above 100 Hz. A detailed discussion of this overall approach may be found in Reference 8.

Control frequency errors are studied using a closed-loop time-domain simulation of the control system. A nonlinear, digital, three-axis control simulation computer program (DTACS) is used to obtain the image position at the f/24 focus as a function of time. The higher frequency vibration errors are studied using an open-loop frequency-domain simulation of the actuator output vibrations exciting the LST structure. The vibration analysis program (VAP) is a linear, digital, three-axis simulation used to obtain image motions versus excitation frequency.

The postprocessor methodology was applied in selecting critical modes of LST Model 1 for DTACS and VAP and comparing these mode orderings with those obtained by conventional techniques. With the low-frequency control option, the postprocessor mode ordering for LST Model 1 was based on image-plane coefficients calculated using the optical amplification matrix (Equation 12). The conventional ordering was based on the product of mode shapes at applied torque and image sensor locations divided by the generalized mass. For the LST structural model, the conventional ordering technique omitted three of the eight critical modes identified by the postprocessor. However, since the modes identified by both techniques are the major contributors to the LST image motion, the postprocessor methodology and the conventional technique are equivalent for this particular simulation.

With the higher-frequency fine-stabilization option, the postprocessor mode ordering for LST Model 1 was accomplished using Equations (13) through (16), where the applied forces and torques were proportional to reaction wheel excitation frequency raised to the 1.7 power. The conventional ordering was again based on the product of input and output mode shapes normalized by the generalized mass. For the LST structural model, the conventional ordering technique omitted 17 of the 20 critical modes identified by the postprocessor. The LST image motions calculated from these two different sets of modes were, of course, significantly different. Those image motions calculated from the conventional ordering were in error by an order of magnitude compared with those from the postprocessor ordering.

The preprocessor methodology was applied in generating LST Model 2 with discrete damping components. The critical modes of this model were selected for DTACS and VAP by the postprocessor, and the simulation results using these modes were compared with the previous results from LST Model 1. For the DTACS low-frequency control simulation, the postprocessor mode ordering

and the calculated image motions were essentially identical for the two LST models, despite the fact that the damping of the critical low-frequency modes increased an order of magnitude for LST Model 2. The increased modal damping did not significantly affect the results since the control loop used in both cases was designed to be stable for the lower damping. For the VAP sinusoidal vibration simulation, on the other hand, the modal damping effects are very significant. Although the postprocessor mode orderings were quite similar for the two LST models, comparisons of calculated image motions indicate substantial reductions in response amplitudes due to the increase in modal damping from LST Model 1 to LST Model 2.

The data of LST Model 2 was used to assess the significance of damping (velocity) coupling among the normal modes. The measure used to assess the degree of coupling is the ratio of coupled response to uncoupled response. For the 20 most critical modes of LST Model 2, the maximum assessment ratio is 1.024. For all 100 modes, the minimum assessment ratio is 0.459 for the 68th mode. These data indicate that modal velocity coupling is a potentially significant effect for high-accuracy structural dynamic analysis.

CONCLUDING REMARKS

Methodology developed to improve structural joint modeling for distributed damping and to select critical structural modes for subsequent analytical studies has been successfully demonstrated. The NASTRAN viscous damping capability is adequate to represent the general characteristics of localized structural damping, although special care is required in using the VISC damping element. The preprocessor computer program automatically generates NASTRAN BULK DATA cards required for a specific class of Voigt joint damping models. The postprocessor methodology is sufficiently general to select critical modes for a broad class of subsequent analytical studies. LST studies indicate that modal velocity coupling resulting from damping in discrete structural joints has a potentially significant effect on dynamic responses.

ACKNOWLEDGEMENTS

The work described in this report was sponsored primarily by the George C. Marshall Space Flight Center under NASA Contract NAS8-30655. The work was performed under the technical direction of George L. von Pragenau and Larry A. Kiefling of the MSFC Systems Dynamics Laboratory. The basic LST NASTRAN structural model was developed as part of the Boeing-sponsored Orbiting Telescope Systems program under the direction of C. T. Golden. The control-system and sinusoidal vibration studies were performed by William W. Emsley and Patrick J. Hawkins of the Boeing Aerospace Company.

REFERENCES

Merchant, D. H., and Gates, R.M., "Effect of Damping on Excitability of High-Order Normal Modes", Boeing document D180-18835-1, May 30, 1975

Ungar, E. E., "The Status of Engineering Knowledge Concerning the Damping of Built-up Structures", Journal of Sound and Vibration, Vol. 26, No. 1, January 8, 1973, pp. 141-154

Ungar, E. E., "Energy Dissipation at Structural Joints: Mechanisms and Magnitudes", AFFDL-TDR-64-98, August, 1964

Rodgers, E. J., and Warrington, J. D., "A Survey of Material and Structural Damping", Saturn V/Apollo and Beyond, American Astronautical Society National Symposium, Huntsville, Ala., June 11-14, 1967, Transactions, Volume 3

De Veubeke, B. M. F., "Influence of Internal Damping on Aircraft Resonance", Manual on Aeroelasticity, Part 1, AGARD, October 1968, Chapter 3

Lazan, B. J., Damping of Materials and Members in Structural Mechanics, Pergamon Press, 1968

Goodman, L. E., and Klumpp, J. H., "Analysis of Slip Damping with Reference to Turbine-Blade Vibration", ASME Journal of Applied Mechanics, Vol. 23, September 1956, pp. 421-429

Jacot, A. D., and Emsley, W. W., "Assessment of Fine Stabilization Problems for the LST", AIAA Paper No. 73-881, presented at AIAA Guidance and Control Conference, Key Biscayne, Florida, August 20-22, 1973

Table 1.- DMAP ALTER Statements for
Damping Matrix Formulation

N A S T R A N E X E C U T I V E C O N T R O L D E C K

```

ID    LST, MODES 1
APP    DISPLACEMENT
SOL    3,0
CHKPNT YES
TIME    30
ALTER    28,29
SMA2    ESTM,MPT,ECPT,GPCT,DIT/MGG,BGG/V,Y,HTMASS*1.0/V,N,NOMGG/V,N,NOBGG/
          V,Y,COUPMASS/V,Y,CPBAR/V,Y,CPRDD/V,Y,CPQUAD1/V,Y,CPQUAD2/V,
          Y,CPTRIA1/V,Y,CPTRIA2/V,Y,CPTUBE/V,Y,CPQDPLT/V,Y,CPTRPLT/V,
          Y,EPTRBSC 1
SAVE    NOMGG,NOBGG $
ALTER    74
MATGPR GPL,uset,SIL,MAA//C,N,AS
MATGPR    GPL,uset,SIL,BGG//C,N,G$
ALTER    96
MPYAD    PHIG,BGG,/XX/C,N,1/C,N,1/C,N,0 $
MPYAD    XX,PHIG,/BHH/C,N,0/C,N,1/C,N,0' $
CHKPNT    BHH $
MATPPN    BHH,yyy// $
ENDALTER
CEND

```

Table 2.- Basic Structural Dynamic Model Description

Substructure	No. of Gridpoints*	No. of Structural Elements			No. of Dynamic D.O.F.
		Plate	Bar	Scalar Spring	
SM Aft Shell	49	45	32		24
SM Equip. Sect.					54
Inner Shell	75	60			
Ring Frames			45		
Longerons			60		
Reaction Wheels	4		16		24
Shuttle Attach.	4		8		
Forward SSM Shell	12		11		33
IGA	12		10	12	24
Solar Arrays	20		18	12	48
OTA/SI-SSM Interface & Backup	6		9	6	
Telescoping Truss	32		80		48
Secondary Mirror & Support	13		12		6
Primary Mirror & Support	40		53		42
Focal Plane Struct.	19		48		24
SI	1		1		
	<u>287</u>	<u>105</u>	<u>403</u>	<u>30</u>	<u>327</u>

Permanent SPC Gridpoints Excluded

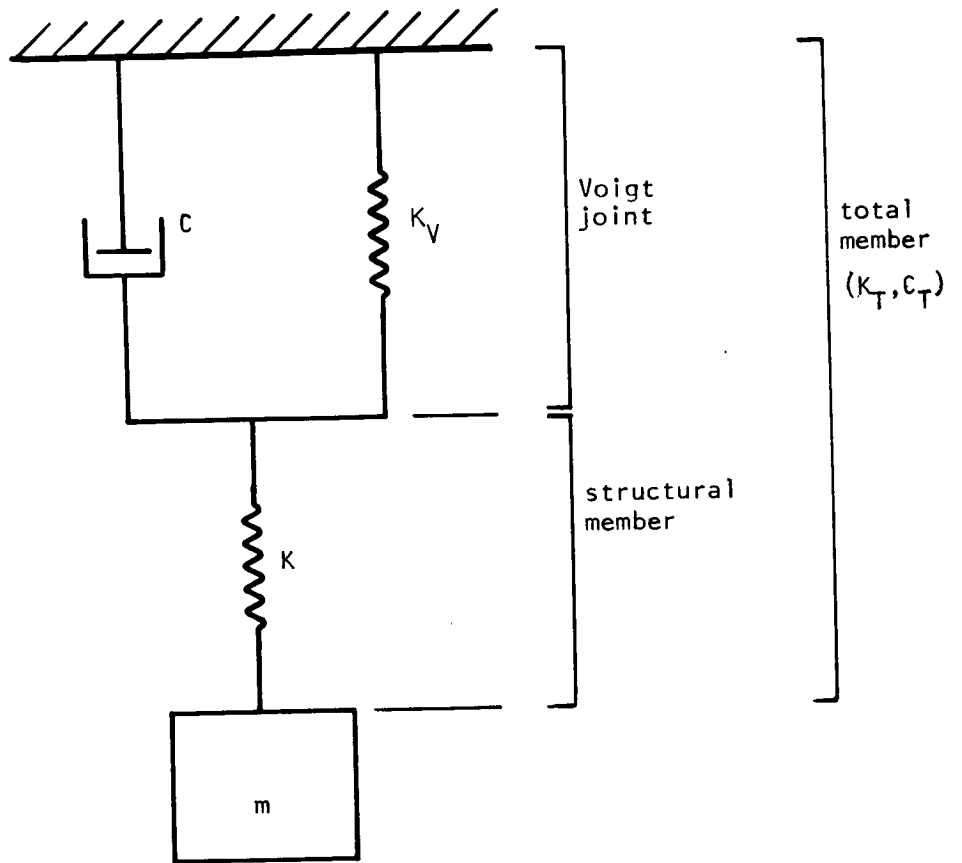


Figure 1.- Schematic of Single Degree-of-Freedom Voigt Joint Model

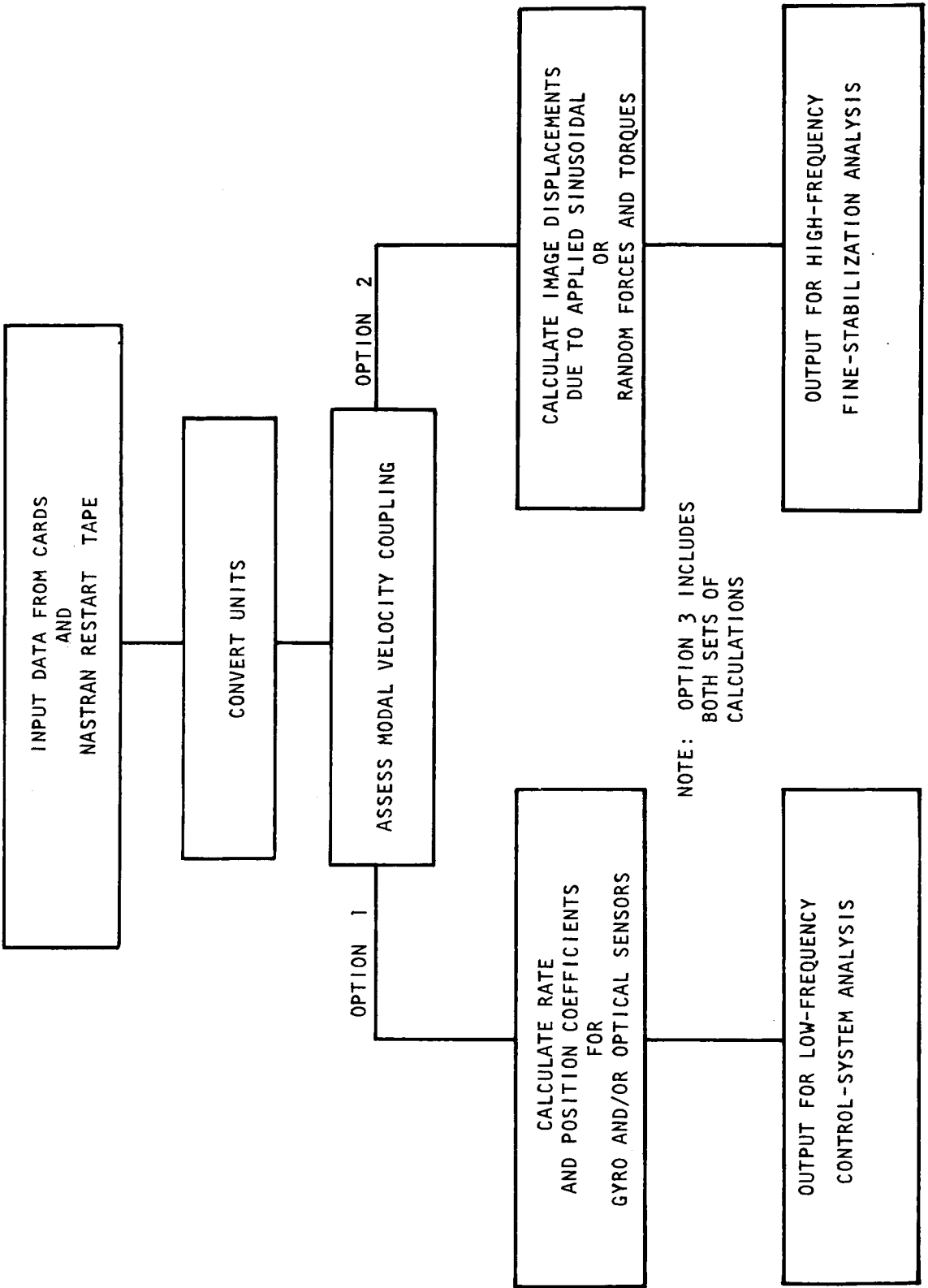


Figure 3.- Postprocessor Program Flow

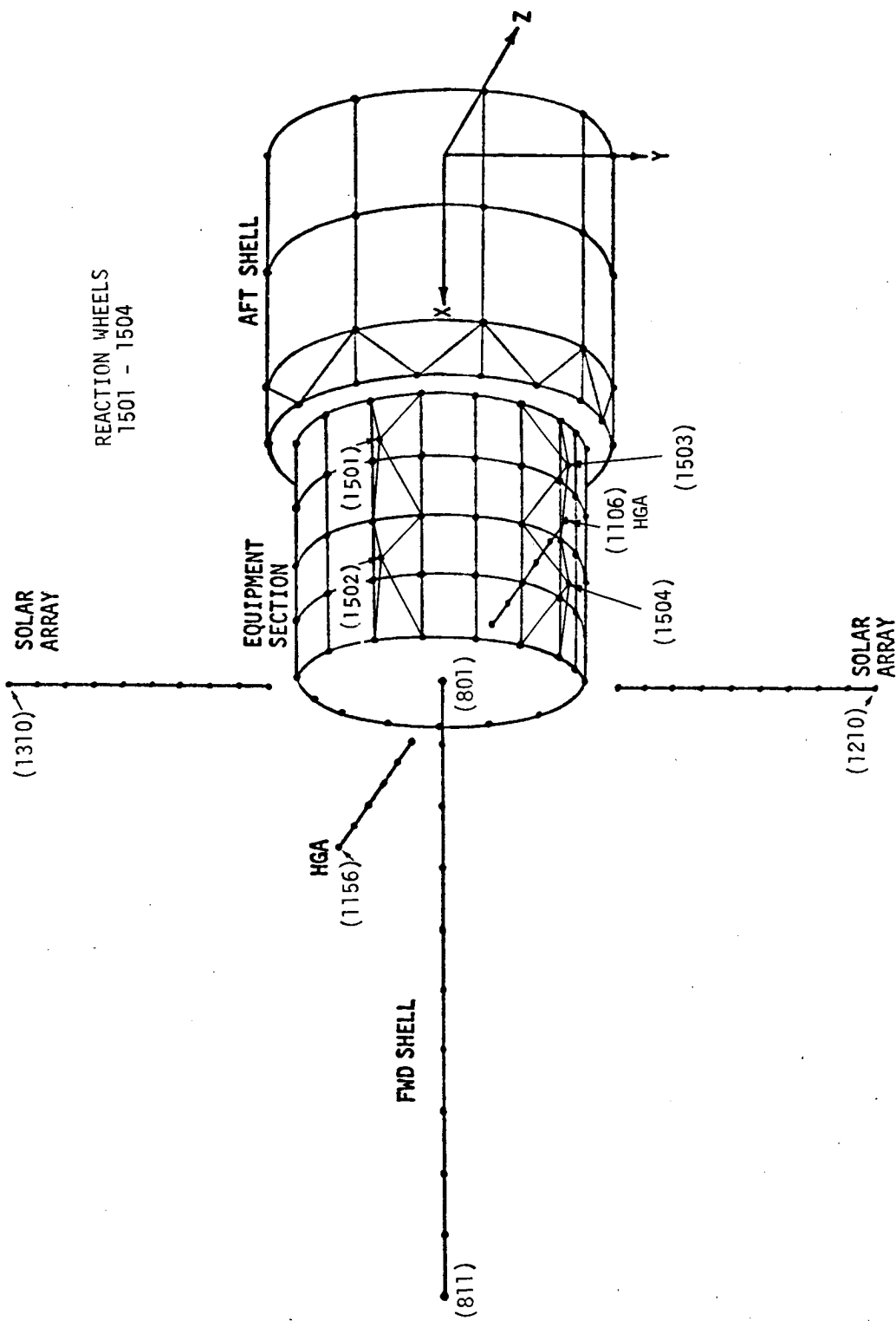


Figure 4.- SSM Finite-Element Model.

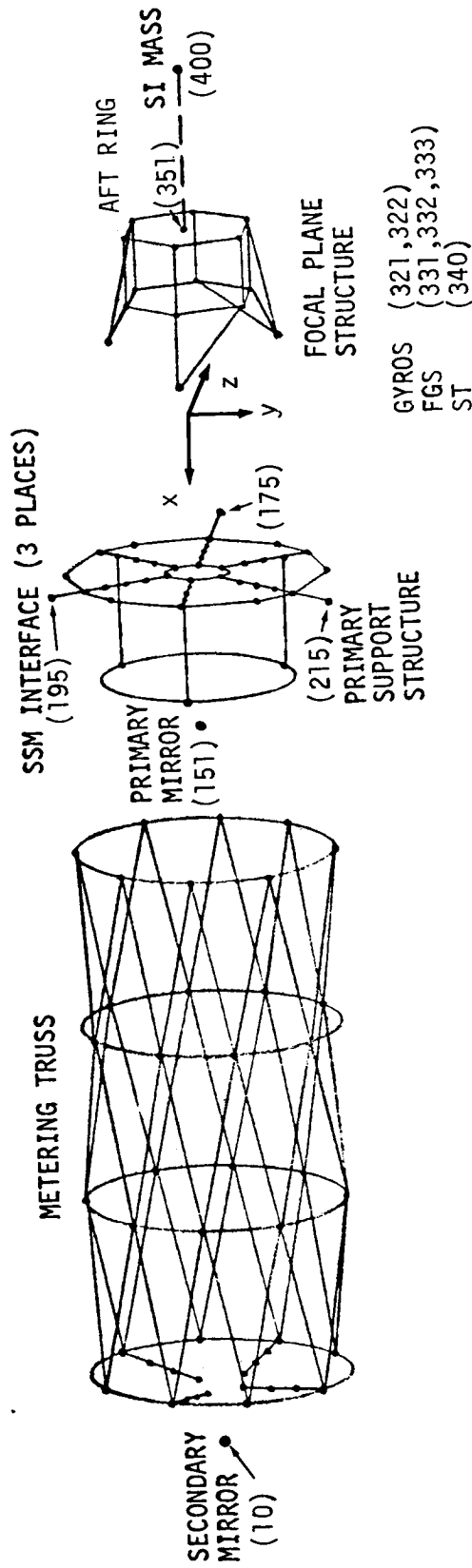


Figure 5.- OTA/SI Math Model.